Research Article Vol. 32, No. 19 / 9 Sep 2024 / *Optics Express* 33208

Optics EXPRESS

Flexible wearable fiber optic sensor for real-time human breath monitoring based on Fabry-Perot interferometer with agar film

GUOXIN SHI,[1] WENWEN WANG,[1] YINGKUAN GUO,[1] JINGSHUN PAN,[2] DANDAN SUN,[1,4] AND JIE MA[1,3,5]

[1] *School of Physics and Electronic Engineering, Shanxi University, Taiyuan 030006, China*
[2] *Guangdong Provincial Key Laboratory of Nanophotonic Functional Materials and Devices, South China Normal University, Guangzhou 510006, China*
[3] *Collaborative Innovation Center of Extreme Optics, Shanxi University, Taiyuan 030006, China*
[4] *sundd@sxu.edu.cn*
[5] *mj@sxu.edu.cn*

Abstract: A flexible wearable sensor based on the Fabry-Perot (FP) structure for human breath monitoring is proposed and demonstrated. This sensor is constructed by fusing a single-mode optical fiber to a small section of capillary and coating the end with agar film. In high relative humidity (RH) environments, the agar film absorbs moisture from the air, which leads to a change in the length of the FP cavity to cause a shift in the interference spectrum. The sensor has a sensitivity of 0.95 nm/%RH for testing RH in the range of 60%RH to 85%RH. The temperature sensitivity of the sensor varies nonlinearly from 30°C to 90°C, averaging 0.34 nm/°C over the range of 30°C to 55°C and 0.06 nm/°C over the range of 60°C to 90°C. The temperature and RH crosstalk problems can be solved by using cascaded fiber Bragg grating followed by matrix operations to monitor temperature and RH parameters simultaneously. In addition, the sensor has a fast response time of 0.88 s and a recovery time of 1.17 s for human breathing. The normal and deep breathing of nine subjects are monitored using the sensor, demonstrating that the sensor is able to recognize normal and deep breathing accurately. The success of this sensor proves that it is feasible to develop sensors with good resistance to vibration interference, good repeatability and high stability for human breath monitoring, which is of great significance for research on human breath monitoring.

1. Introduction

Wearable flexible sensors have garnered significant attention due to their immense potential in biomedical applications and health monitoring [1]. Current wearable devices include the sensing and detecting of various physical and biochemical information such as breathing [2], pulse [3], motion sensing [4], joint activities [5], and human-machine interaction [6]. Among these, the breath monitoring stands out as a crucial factor in assessing physiological status, offering valuable insights into heart, neurological, and pulmonary diseases. The breath monitoring is important during certain imaging and surgical procedures. Patients requiring sedation or anesthesia may suffer breathing failure, which is difficult to predict and can be life-threatening within minutes [7]. Electronic breathing sensors based on capacitive or piezoresistive devices are not suitable in certain situations [8], for example, when the patient is in a magnetic resonance imaging (MRI) system or during oncology treatments that require radiation therapy or high electric/magnetic field treatments. Therefore, the development of a sensor has the advantages of being small in size, highly flexible, robust against interference, and biocompatible is of great significance and a great challenge.

#535272
Journal © 2024

https://doi.org/10.1364/OE.535272
Received 12 Jul 2024; revised 13 Aug 2024; accepted 14 Aug 2024; published 29 Aug 2024

The emergence of optical sensors provides a new alternative. Particularly in recent years, optical fiber sensors with broadband, remote transmission, and multi-parameter functionalities offer a range of unique advantages including corrosion resistance and immunity to electromagnetic interference, promising extensive application prospects [6]. Various optical fiber sensors have been reported for measuring relative humidity (RH) [9], temperature [10], refractive index [11], and biosensing [12]. In 2017, Bobo Du et al. have designed a full-optical fiber breathing sensor using etched single-mode fiber coated with MoS_2, which has an excessively long recovery time [13]. In 2020, Jing Yang et al. have investigated a highly sensitive humidity sensor based on a gelatin-coated side-polished fiber-optic directional coupler for human breath monitoring, without eliminating the cross-over effects of vibrations generated during breathing [14]. In 2022, Mingpan Bi et al. have developed a highly sensitive humidity sensor by combining Nb_2CT_X nanosheets with microfibers, which does not exclude the cross-effect of temperature [15]. In 2024, Yuzhuo Li et al. have introduced a fiber-optic humidity sensor for human breath monitoring using multimode interference and Mach-Zönder interference, which has an excessively long recovery time [16]. In the same year, Yaxun Zhang et al. have presented a Fabry-Perot interferometer (FPI) fiber sensor based on sealed liquid glycerol microcavity for human breath monitoring [17]. Studies have shown that FPI humidity sensors typically fill humidity-sensitive materials in hollow fibers. Some Fabry-Perot (FP) cavities have been developed with agar membranes [18], chitosan membranes [19], polyvinyl alcohol membranes [20], hydrogel membranes [21], and other materials. Among them, agar is a substance with coagulation and thickening properties, stable chemical properties, and is widely used in food engineering, daily chemical engineering, biomedical and other fields [22]. The hygroscopicity of agar is one of its most remarkable properties, thus in environments with high RH, agar can absorb moisture from the air, causing it to expand in volume and soften its texture. At the same time, agar has coagulation and thickening properties, making it easy to form a stable membrane, thereby forming a stable FP structure [23,24]. Therefore, the combining agar moisture-sensitive materials with FP can provide a high-sensitivity platform for human breath monitoring.

In this research, a flexible wearable sensor base on a Fabry-Perot structure for human breath monitoring is presented. The sensor is assembled from a capillary tube and a single-mode optical fiber, with the other end of the capillary tube immersed in an agar solution to form an agar film. Due to the ability of the agar membrane to absorb moisture from the air in high RH environments, the length of the FP cavity changes, resulting in a shift in the interference spectrum. Three sensing experiments are conducted in the RH range of 60%RH-85%RH with a sensitivity of 0.95 nm/%RH. Because agar exhibits sol-gel transition characteristics sensitive to temperature, the temperature sensitivity of the sensor is nonlinear over the temperature range of 30°C to 90°C. The temperature sensitivity of the sensor averages 0.34 nm/°C in the range of 30°C to 55°C, and the temperature sensitivity of the sensor averages 0.06 nm/°C in the range of 60°C to 90°C. In addition, to address the issue of temperature and RH crosstalk, a cascaded FBG is used to track wavelength shifts of the interference spectrum, followed by matrix operations to measure RH and temperature simultaneously. The sensor performance test shows that the sensor can exclude the vibration cross-influence, and has good repeatability and stability. The sensor has a fast response and recovery time (0.88 s – 1.17 s). The normal and deep breathing in nine subjects used this sensor are monitored. The data shows that every subject has a mean response time of 0.88 s and a recovery time of 1.17 s in normal breathing, meanwhile, in deep breathing, the mean response time is 1.07 s and the recovery time is 1.36 s. The monitoring of the breathing patterns shows that the proposed breath sensor has high repeatability, reliability and effectiveness, which opens up the possibility of developing new flexible wearable sensors.

2. Experimental section

2.1. Regents and instruments

Agar powder ($C_{12}H_{18}O_9$, ask ≤ 1.5‰) was purchased from Macklin Biochemistry Co., Ltd (Shanghai, China). Preparation of solutions used deionized water, which was obtained from an ultrapure water system. The sensor comprised single-mode fiber (SMF, Corning SMF-28e$^+$) and capillary (TSP075150, 75 µm inner diameter, and 150 µm outer diameter with the protective layer). The cross-sectional images and macroscopic structures of capillary before and after the dip-pulling into the solution were observed using an optical microscope (Caikon DMM-200C), and the reagents required for the experiments were prepared using a magnetic stirrer (MS-280-H).

The instruments used to monitor the sensing performance of the probe towards RH and temperature include an amplified spontaneous emission source (ASE, range of 1528-1603 nm, power of 10 dBm), an optical spectrum analyzer (OSA, Anritsu MS9740A, range of 600-1700nm), a fiber fusion splicer (Fujikura 87S+), an optic-fiber cutter (Fujikura CT50), a programmable climate chamber (HWS-30), and a column temperature chamber (HT-330), etc. The instruments used for breath monitoring include a tunable laser (Agilent 81682B, range of 1460-1580 nm, accuracy of ±0.01 nm), a photodetector (PD, KG-HSP-1200-SM-FA), oscilloscope (OSC, UNI-T MSO7204X, bandwidth of 2 GHz, sampling rate of 10 GSa/s), and electromagnetic shaker (JY-H-200) etc.

2.2. Sensor fabrication

The structure of the sensor designed for breath monitoring is shown in Fig. 1(a, top), which consists of a Bragg grating and a Fabry-Perot structure. The process of fabricating the sensor is divided into six steps. The first step is to make an agar powder solution to prepare for the subsequent dipping. 10 mL of deionized water and 0.05 g of agar powder are added to a beaker. Then, the agar powder solution is placed on a magnetic stirrer and stirred at 500 rpm/min for 20 min (the temperature maintained at 80°C) until the agar powder is completely dissolved and evenly dispersed. The second step is to remove the protective metal layer around the hollow capillary by the combustion method. The inner and outer diameters of the capillary cross-section are shown in Fig. 1(b, top). In the third step, a single-mode fiber and capillary are manually spliced together through a fiber fusion splicer. To prevent the collapse of the hollow capillary, we choose the arcing condition of -10 bits for power and 400 ms of a fiber fusion splicer. In the fourth step, the other side of the fused capillary is cut using a fiber cutter to obtain the desired capillary length (the experimentally fabricated capillary length of 180 µm). In the fifth step, the capillary is operated by an automatic stepper motor to dip it into the agar solution and pull it out. The dipping time is controlled to be 2 s each time to ensure the film thickness of roughly 10 µm. Figure 1(b, top) shows the optical microscope cross-sectional images of the capillary before and after the dip-pulling into the solution (agar solution concentration of 0.005 g/ml). The prepared sensors are precipitated for 2 h to make the structure of the films more stable. Figure 1(b, bottom) shows an optical microscope image of the sensor with a capillary length of 180 µm as well as the corresponding interference spectrum. Finally, the sensor is secured inside the nasal oxygen tube to create an ideal environment for detection, as shown in Fig. 1(a, bottom).

2.3. Sensing principle

As shown in Fig. 1(a, top), the fabricated sensor has three reflective surfaces M_1, M_2 and M_3, where M_1 is the reflective surface of the single-mode fiber and air, M_2 is the reflective surface of air and agar film, and M_3 is the reflective surface of the agar film and external air. Due to the complex structure of the sensitive material, the actual sensor approximates two-light interference, where the incident light emits complex scattering and reflection, resulting in the actual reflected

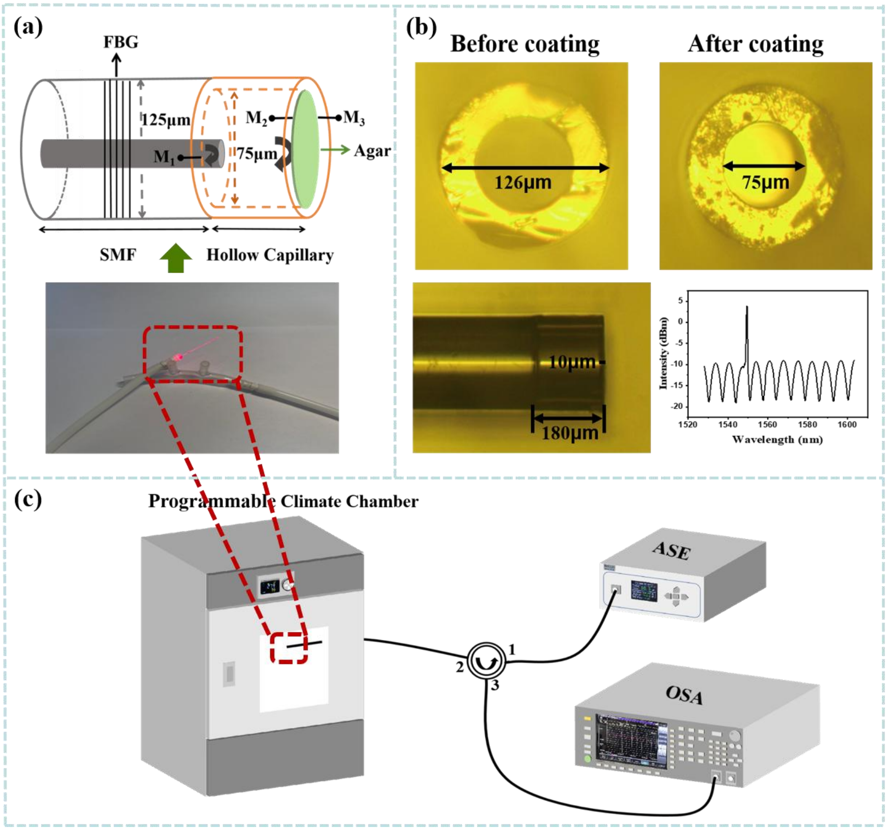

Fig. 1. (a) Structure diagram of the sensor and real photograph encapsulated in a nasal oxygen tube. (b) (top) The cross-section of the capillary before and after the dip-pulling into the solution. (bottom) microscope image of capillary length and corresponding interference spectrum. (c) Experimental setup for the relative humidity sensing experiments.

light involved in the interference being mainly single-mode fiber-air and air-agar film to form the FP cavity.

From the theory of interference of light, the intensity of light formed by the interference of two beams of reflected light can be expressed as:

$$I = I_0 \left[R_1 + R_2 + 2\sqrt{R_1 R_2} cos \left(\frac{2\pi d}{\lambda} + \varphi \right) \right] \tag{1}$$

where I_0 is the intensity of the incident light, R_1 and R_2 represent the reflectivity of the single-mode fiber and air and the reflectivity of the interface between the air and the agar film, respectively [25,26]. λ is the wavelength, d is the optical range difference between the two beams of light, and φ is the initial phase. When the reflectivity of the two reflective surfaces R_1 and R_2 is larger, the interference spectrum is clearer and sharper, and the spectral resolution is higher. The fineness F can be expressed as:

$$F = \frac{\pi \cdot \sqrt[4]{R_1 R_2}}{1 - \sqrt{R_1 R_2}} \tag{2}$$

According to Eq. (2), the reflectance R_1 and R_2 are positively correlated with the corresponding spectral fineness F without considering the loss in the FP cavity, and the reflectance R_1 and R_2 of the two reflective surfaces are expressed as:

$$\begin{cases} R_1 = \frac{(n-n_1)^2}{(n+n_1)^2} \\ R_2 = \frac{(n_1-n_2)^2}{(n_1+n_2)^2} \end{cases} \tag{3}$$

In the formula, n, n_1 and n_2 represent the refractive indices of the medium inside the FP cavity, the single-mode fiber core and the agar film, respectively. When the medium in the cavity is air, the refractive index is approximately equal to 1, which can be calculated to obtain $R_1 \approx 4\%$, and the reflectance of R_2 is also much less than 1. Therefore, the interference spectrum formed has a lower sharpness and the shape is similar to a sinusoidal function. The free spectral range of the interference spectrum can be expressed as:

$$\varDelta\lambda = \frac{\lambda^2}{2nL} \tag{4}$$

where L is the cavity length of the FPI sensor [27]. The wavelength of the trough of the interference spectrum is expressed as:

$$\lambda_m = \frac{4nL}{2m+1} \quad m = 1, 2, 3 \cdots \tag{5}$$

From Eq. (5), λ_m depends on the cavity length L and refractive index n, and its relative change is expressed as:

$$\frac{\varDelta\lambda_m}{\lambda_m} = \frac{\varDelta n}{n} + \frac{\varDelta L}{L} \tag{6}$$

where $\varDelta\lambda_m$ is the change in the wavelength of the trough, $\varDelta n$ is the change in the refractive index, and $\varDelta L$ is the change in the FP cavity length.

So the RH sensitivity of the FPI sensor can be derived as:

$$S_{RH} = \frac{\varDelta\lambda}{\varDelta RH} = \left(\frac{\varDelta n}{\varDelta RH \cdot n} + \frac{\varDelta L}{\varDelta RH \cdot L}\right)\lambda \tag{7}$$

From Eq. (7), it can be concluded that when the RH of the environment around the sensor increases [28,9], the agar film will absorb water and expand, leading to changes in the cavity length and refractive index of the agar film cavity, which will cause a wavelength shift. Therefore, the measurement of ambient relative humidity can be realized by measuring the change in the position of the trough of the sensor's interference spectrum, which allows for real-time monitoring of relative humidity in human breathing.

3. Results and discussion

3.1. Experimental setup

Figure 1(c) shows the experimental setup for the relative humidity sensing experiments. Light from the ASE is propagated through an optic fiber circulator to the sensing head for reflection, and the light reflected is recorded by an OSA with a wavelength resolution of 0.03 nm. As shown in Fig. 1(c), the prepared sensing probe encapsulated in a nasal oxygen tube (Fig. 1(a, bottom)) is placed in a programmable climate chamber with a resolution of 0.1% RH. The sensing probe is fixed inside the box using the fiber optic fixture, which is shielded with a windshield to prevent airflow inside the box from blowing directly to the probe. To eliminate the effect of temperature fluctuations on the testing results, the temperature is maintained at approximately 25°C throughout the testing period.

3.2. Relative humidity testing

The sensor encapsulated in the nasal oxygen tube is subjected to RH testing in the range of 60%RH-85%RH in steps of 5%RH, and the wavelength shift of the interference spectrum is monitored and recorded. Figure 2(a) shows the wavelength shift of the interference spectrum of the sensing probe as RH increases, and it can be observed that the interference spectrum exhibits a red shift when the RH increases within the range of 60%RH-85%RH. To verify the reproducibility of the sensor, we test the sensor for RH at intervals of 1, 3 and 7 days and perform a linearity analysis. Figure 2(b) shows a plot of the results of the repeated experiments. With increasing RH, the sensor exhibits a wavelength shift sensitivity of 0.95 nm/%RH and a linearity of 0.9879. The above experimental results confirm the good reproducibility of the sensor and verify that the agar powder material is not damaged by water solubility, which suggests that the proposed Fabry-Perot structure is finally believed to be stable. Figure 2(c) shows the monitoring of the FBG spectral position during the RH test. Due to its optical fiber material and working principle of FBG, it is sensitive only to temperature and unaffected by RH changes. According to the data results, the spectral position is approximately 1549.4136 nm with no fluctuation, indicating that the test process is not affected by temperature. The temperature during the RH test can be calibrated by monitoring the FBG spectral position.

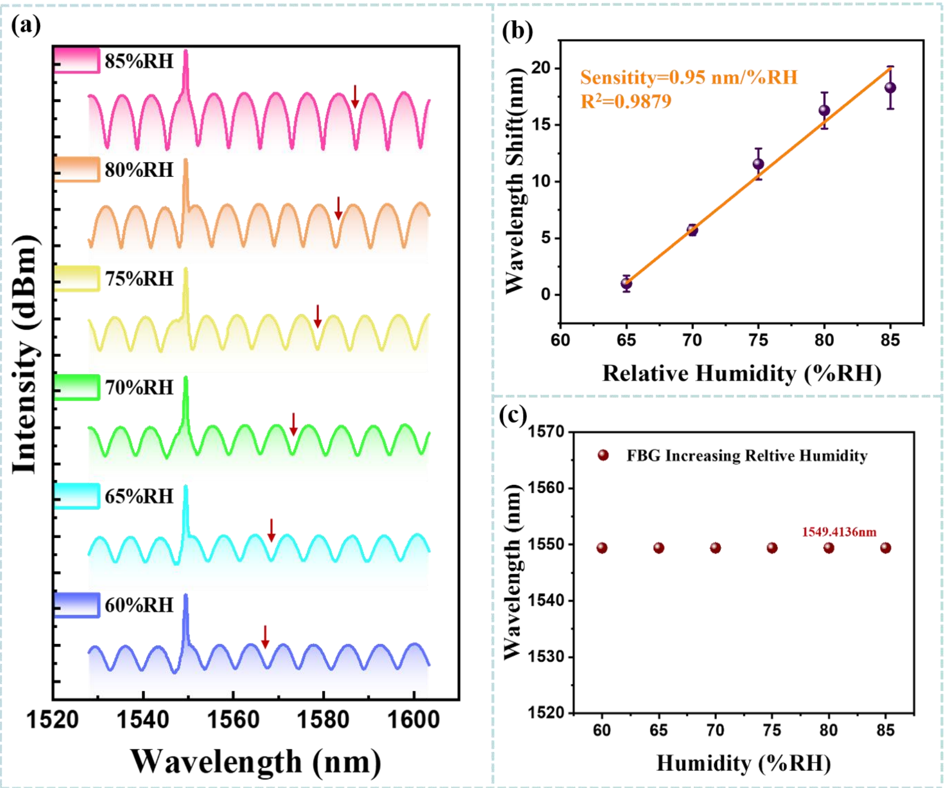

Fig. 2. RH test on a sensing probe encapsulated in a nasal oxygen tube. (a) Interference spectrum with increasing humidity. (b) Repeated experimental results of the sensor. (c) Data analysis results of humidity increase test on FBG.

3.3. Temperature testing

To address the issue of RH and temperature crosstalk, the response to the temperature of the sensor must be evaluated. Therefore, temperature testing of sensors encapsulated in nasal oxygen tubes is performed in the range of 30°C to 90°C in steps of 5°C. For the temperature testing, we set the RH to 60%RH. Figure 3(a) shows the wavelength redshifts of the interference spectrum of the sensing probe as the temperature increases. To verify the repeatability of the sensor, the sensor tests for the temperature at intervals of 1, 3 and 7 days, and the nonlinear analysis is performed. Figure 3(b) shows a plot of the repeated results of the experiments. The temperature sensitivity of this sensor averages 0.34 nm/°C in the range of 30°C to 55°C, and the temperature sensitivity of this sensor averages 0.06 nm/°C in the range of 60°C to 90°C, with an R^2 of 0.9955. The results show that the wavelength shift changes significantly around 45°C (sol-gel transition temperature). The refractive index of the agar and the length of the FP cavity change slightly, resulting in a gradual decrease in the wavelength shift. Figure 3(c) shows the monitoring of the spectral position of FBG during the temperature test. The results show that the spectral position of FBG (1549.4136 nm) red-shifts with increasing temperature. The temperature sensitivity of the FBG is 0.01 nm/°C with R^2 of 0.9987. Thus, FBG is sensitive to temperature.

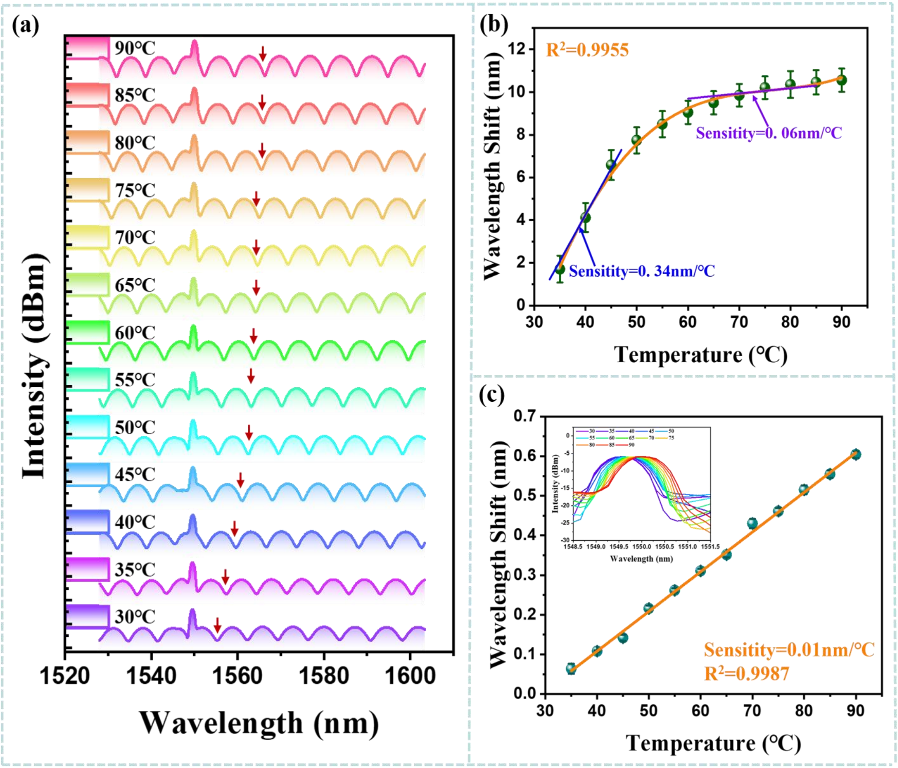

Fig. 3. Temperature test on a sensing probe encapsulated in a nasal oxygen tube. (a) Interference spectrum with increasing temperature. (b) Repeated experimental results of the sensor. (c) Data analysis results of temperature increase test on FBG.

For fiber optic sensors, the study of temperature cross-sensitivity is very important, which together with relative humidity affects the change in the wavelength of the transmission spectrum. Therefore, the actual test results must be compensated and adjusted accordingly. Assuming that

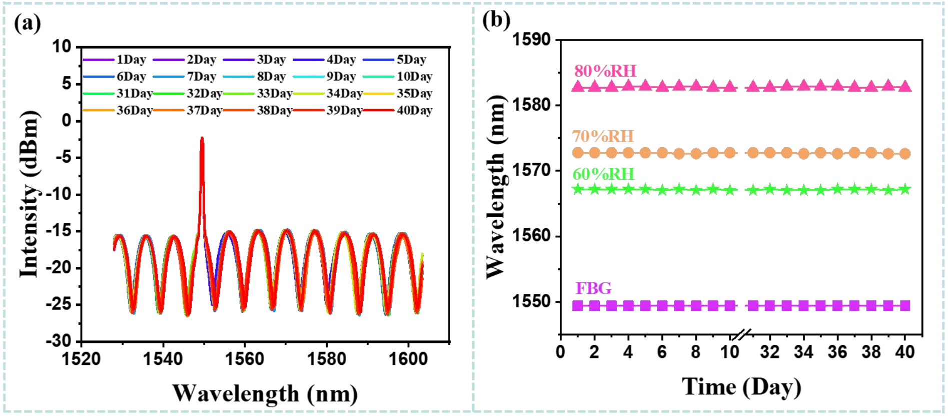

Fig. 4. Stability RH tests performed on the sensor. (a) Variation of interference spectrum and FBG spectral position. (b) Results of data analysis for stability tests performed for RH of 60%RH, 70%RH, 80%RH and FBG spectra.

the fiber optic sensor is affected by n external parameters, that is:

$$\varDelta X = \begin{bmatrix} \varDelta X_1 \\ \vdots \\ \varDelta X_n \end{bmatrix} \tag{8}$$

where $\varDelta X_i (i = 1 \ldots n)$ represents each physical parameter. $\varDelta Y$ is the variation of optical parameters, such as intensity, wavelength, frequency, etc., which obtained from measurements. A matrix can be established between the variation of the optical parameter $\varDelta Y$ inside the sensor and each external parameter:

$$\varDelta Y = \begin{bmatrix} \varDelta y_1 \\ \vdots \\ \varDelta y_n \end{bmatrix} = \begin{bmatrix} k_{x_{1,1}} & \cdots & k_{x_{n,1}} \\ \vdots & \ddots & \vdots \\ k_{x_{1,n}} & \cdots & k_{x_{n,n}} \end{bmatrix} \begin{bmatrix} \varDelta x_1 \\ \vdots \\ \varDelta x_n \end{bmatrix} \tag{9}$$

The inverse of matrix K is calculated to obtain the measured physical parameter as [29]:

$$\varDelta X = K^{-1}\varDelta Y = \frac{K^*}{|K|}\varDelta Y \tag{10}$$

During human breath monitoring, the temperature in the nasal cavity will change slightly. Therefore, when the temperature and RH change at the same time, the wavelengths of FPI and FBG will be shifted, and the wavelength shift can be expressed as:

$$\begin{bmatrix} \varDelta\lambda_{FPI} \\ \varDelta\lambda_{FBG} \end{bmatrix} = \begin{bmatrix} K_{1,T} & K_{1,H} \\ K_{2,T} & K_{2,H} \end{bmatrix} \begin{bmatrix} \varDelta T \\ \varDelta RH \end{bmatrix} \tag{11}$$

where $\varDelta\lambda_{FPI}$ and $\varDelta\lambda_{FBG}$ are the wavelength shifts of FPI and FBG, $\varDelta T$ and $\varDelta RH$ are the temperature and RH variations, $K_{1,T}$ and $K_{2,T}$ are the temperature sensitivities of FPI and FBG, and $K_{1,H}$ and $K_{2,H}$ are the RH sensitivities of FPI and FBG [30–32].

Equation (11) can be calculated from the cross matrix as:

$$\begin{bmatrix} \Delta T \\ \Delta RH \end{bmatrix} = \begin{bmatrix} K_{1,T} & K_{1,H} \\ K_{2,T} & K_{2,H} \end{bmatrix}^{-1} \begin{bmatrix} \Delta\lambda_{FPI} \\ \Delta\lambda_{FBG} \end{bmatrix} = \frac{1}{K_{1,T}K_{2,H} - K_{1,H}K_{2,T}} \begin{bmatrix} K_{2,H} & -K_{1,H} \\ -K_{2,T} & K_{1,T} \end{bmatrix} \begin{bmatrix} \Delta\lambda_{FPI} \\ \Delta\lambda_{FBG} \end{bmatrix} \quad (12)$$

In the range of 30°C to 55°C, the temperature test data of $K_{1,T1} = 0.34\ nm/°\mathrm{C}$ and $K_{2,T1} = 0.01\ nm/°\mathrm{C}$ can be known from Fig. 3(b) and Fig. 3(c). The RH test data of $K_{1,H1} = 0.95\ nm/\%RH$ and $K_{2,H1} = 0\ nm/\%RH$ can be known from Fig. 2(b) and Fig. 2(c) [33]. The above values are substituted into Eq. (12). The final analytical expression for this matrix is:

$$\begin{bmatrix} \Delta T_1 \\ \Delta RH \end{bmatrix} = \frac{1}{-0.0095} \begin{bmatrix} 0 & -0.95 \\ -0.01 & 0.34 \end{bmatrix} \begin{bmatrix} \Delta\lambda_{FPI} \\ \Delta\lambda_{FBG} \end{bmatrix} \quad (13)$$

In the range of 60°C to 90°C, the temperature test data of $K_{1,T2} = 0.06\ nm/°\mathrm{C}$ and $K_{2,T2} = 0.01\ nm/°\mathrm{C}$ can be known from Fig. 3(b) and Fig. 3(c). The RH test data of $K_{1,H2} = 0.95\ nm/\%RH$ and $K_{2,H2} = 0\ nm/\%RH$ can be known from Fig. 2(b) and Fig. 2(c). The above values are substituted into Eq. (12). The final analytical expression for this matrix is:

$$\begin{bmatrix} \Delta T_2 \\ \Delta RH \end{bmatrix} = \frac{1}{-0.0095} \begin{bmatrix} 0 & -0.95 \\ -0.01 & 0.06 \end{bmatrix}^{-1} \begin{bmatrix} \Delta\lambda_{FPI} \\ \Delta\lambda_{FBG} \end{bmatrix} \quad (14)$$

Based on Eq. (13) and Eq. (14), this sensor can realize the simultaneous measurement of RH and temperature by a simple calculation, which is used to solve the temperature crosstalk during human breath monitoring.

3.4. Stability test

To test the stability of the sensors, the RH testing is carried out over a period of 20 days (10 days first, then 10 days after 30 days) at constant temperature and RH. To facilitate the application of actual breathing scenarios, the test RH is 60%RH, 70%RH and 80%RH with the test temperature of 37°C. Figure 4(a) shows the variation of the interference spectrum and the FBG spectrum over a long period at RH of 60%RH. Figure 4(b) shows the wavelength response of the sensor at RH stabilization values of 60%RH, 70%RH and 80%RH, respectively. The results show that the maximum value of wavelength fluctuation of the sensor is only 0.1508 nm during the test, and the corresponding accuracy error of RH testing is ±0.16%RH. There is no fluctuation in the spectral position of the FBG, which indicates that the RH testing process is not affected by temperature, so the sensor has good stability.

3.5. Breath monitoring

We combine FPI sensors and nasal oxygen tubing to perform human breath monitoring, mainly to test the sensors' response under normal and deep breathing conditions. As shown in Fig. 5(a), the experimental setup for human breath monitoring by volunteers wearing nasal oxygen tubes with integrated FPI sensors is demonstrated (see Visualization 1), as well as a red light test figure of the sensor. The light from the tunable laser propagates through an optic fiber circulator to the sensing head for reflection and the reflected light is received by the PD. The PD converts changes in the output optical power into an electrical signal, which is then sent to an oscilloscope to display and record the breathing changes in real time.

To verify the effect of external factors (e.g., airflow, vibration) on the sensor during the actual detection process, it is necessary to test the responsiveness of the sensor to vibration. Figure 5(b)

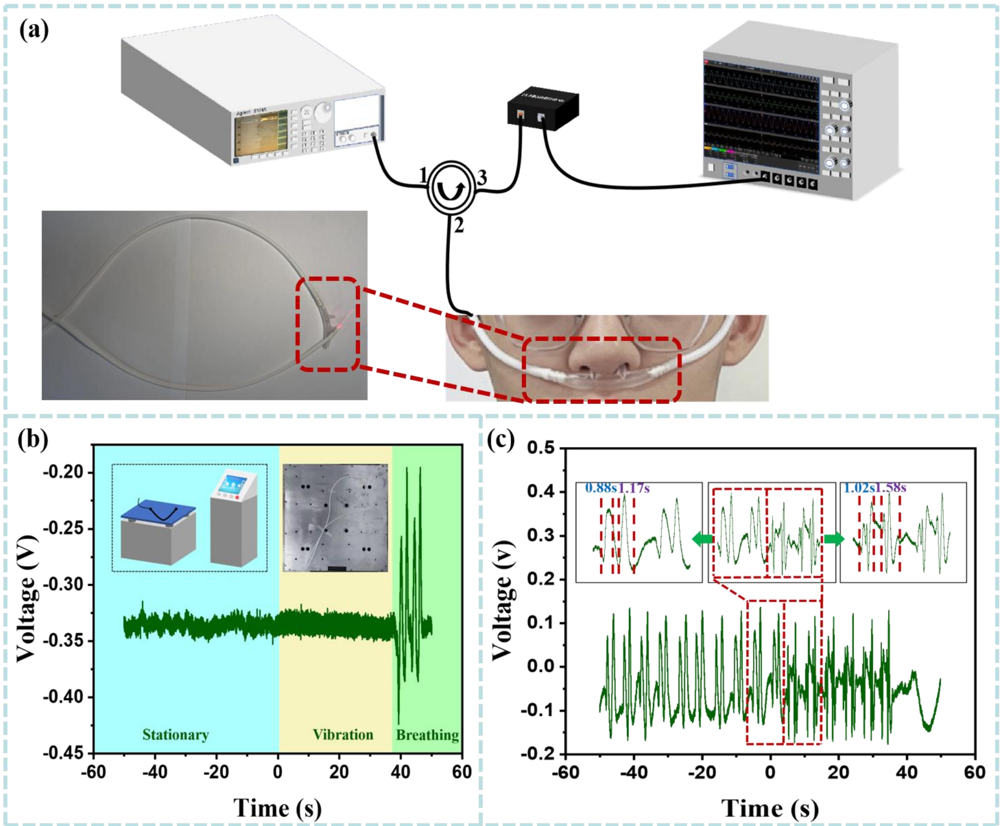

Fig. 5. Integrating sensors into a nasal oxygen tube to monitor human breathing. (a) Schematic of the experimental setup for human breath monitoring and red light test figure after sensor encapsulation. (b) Response of the sensor under stationary, vibration, and breathing conditions. (c) A volunteer performing breath monitoring at different breathing depths and observing reactions and recovery times by amplifying both normal and deep breathing states.

shows the response of the sensor under stationary, vibration and breathing conditions. As shown in the schematic in the left inset of Fig. 5(b) and the real photograph in the right inset of Fig. 5(b), the sensor is placed on a vibration table and test at a vibration frequency of 10 Hz. The experimental data indicate no significant changes during the stationary state from −50 s to 0 s and the vibrating state from 0 s to 37 s. However, the significant breathing activity can be observed from 37 s to 50 s. The experimental results show that the difference between the vibration state and the stationary state is not significant, while the difference between the vibration state and the breathing state is very significant. These results indicate that the sensor is not affected by external factors such as vibrations and has a high anti-interference capability during the breath monitoring process.

Figure 5(c) shows a volunteer performing breath monitoring at different breathing depths, focusing on the response and recovery times of the sensor under normal and deep breath conditions. The middle inset of Fig. 5(c) illustrates the results of a transition experiment from normal to deep breathing as shown in the dashed box (see Visualization 1). In addition, the left inset of Fig. 5(c) shows the results of a scaled-up experiment for a normal-breathing test in which the sensor's breathing response time is 0.88 s and the recovery time is 1.17 s. In contrast, the right

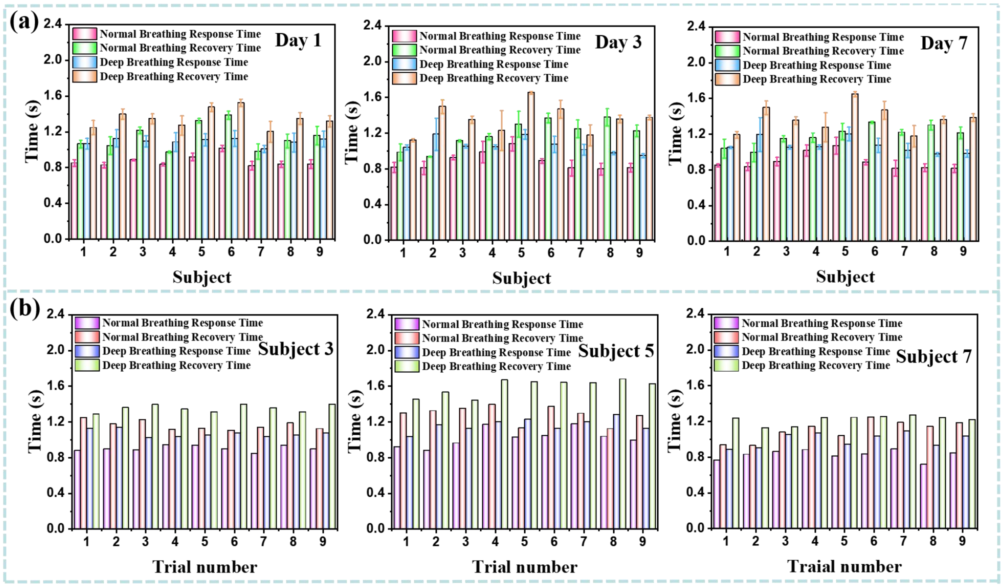

Fig. 6. Multi-person breath monitoring tests (nine subjects). (a) The bar chart of the repeatability test for the response and recovery times of normal and deep breathing monitored by the sensor on 1, 3, and 7 days. (b) Breath monitoring data plots for Subjects 3, 5, and 7 are selected from the following data.

inset of Fig. 5(c) shows the results of a scaled-up experiment for a deep-breathing test in which the sensor's breathing response time is 1.02 s and the recovery time is 1.58 s. As can be seen in the enlarged images of Fig. 5(c), the recovery time of the breath test is longer than the response time, with the sensor's recovery time being 33% slower than the response time during normal breathing, and the sensor's recovery time being 55% slower than the response time during deep breathing. This is due to the hysteresis effect of the material stress, which makes the overall recovery time longer and also has an effect on the fast response performance of the sensor.

To further evaluate the response characteristics of the sensor to different breathing depths, the reproducibility test for the sensor's performance in breath monitoring is designed and conducted. In this test, the results of the response time and recovery time for breath monitoring of nine subjects (Subjects 1, 2, 3 and 4 are male lean body types, Subjects 5 and 6 are male strong body types, and Subjects 7, 8, and 9 are female normal body types.) using this sensor are shown in Fig. 6(a). Each subject undergoes three breath monitoring tests on 1, 3, and 7 days. The nasal oxygen tube integrated with the FPI sensor is inserted into the subjects' nostrils, and the tubes on both sides of the nasal oxygen tube are hung over the ears, which is adjusted to a comfortable position. The participants first breathe normally and then take deep breaths. In Fig. 6(a), the response time for normal breathing is approximately 0.88 s with the recovery time of about 1.17 s, whereas the response time for deep breathing is around 1.07 s with the recovery time of approximately 1.36 s. The experimental data show that the recovery time of the breathing test is longer than the response time. This is because of the hysteresis effect of material stress, thereby prolonging the overall recovery time. Both the response time and recovery time for deep breathing are longer than those for normal breathing because, during deep breathing, the expansion and contraction amplitude of the lungs and chest cavity is larger, which causing the sensor to take more time to recover. As shown in Fig. 6(b), the data from nine breath tests for Subjects 3, 5, and 7 are analyzed. In normal breathing of Subjects 3, 5 and 7, the average values of response time are 0.90 s, 1.02 s and 0.82 s respectively, and recovery time are 1.16 s, 1.28

s, 1.09 s respectively. In deep breathing, the average values of response time is 1.06 s, 1.16 s, 0.99 s respectively, and recovery time is 1.35 s, 1.59 s, 1.27 s, respectively. The results of the breath data indicate that Subject 5 (a male with a strong body type) exhibits the longest response and recovery times for both normal and deep breathing. In comparison, Subject 3 (a male with a lean body type) has longer response and recovery times for normal and deep breathing than Subject 7 (a female with a normal body type). As the measuring period increases, the sensor maintains good working conditions, demonstrating good reproducibility and high reliability in breath monitoring. Furthermore, due to the small size and flexibility of the FPI sensor, it is also convenient for integration with other wearable devices for breath monitoring. Therefore, our proposed sensor has potential applications in the field of real-world human health monitoring.

Table 1 presents a comparative analysis of the performance of sensors for human breathing monitoring using different fiber optic structures. The results show that our sensors have the advantages of high sensitivity, good stability, faster response time and recovery time. These fully demonstrate the advantages of FPI sensors for use in human breathing monitoring.

Table 1. Performance comparison of sensors based on different fiber optic structures for human breath monitoring

Structure	Material	RH sensitivity	Temperature sensitivity	Vibration effect	Respond time	Recovery Time	Year	Ref.
Etched single-mode fiber	MoS_2	-	-	No	0.066 s	2.395 s	2017	[13]
Side-polished fiber	Gelatin	−7.005 nm/%RH	0.3467 nm/°C	No	2.97 s	1.28 s	2020	[14]
Microfiber interferometer	Nb_2CT_X	−86 pm/%RH	No	No	1.76 s	5.71 s	2022	[15]
Mach-Zehnder interferometer	Gelatin	0.634 nm/% RH	0.105 nm/°C	No	6.293 s	171.062 s	2024	[16]
Fabry-Perot interferometer	Glycerol and ultraviolet adhesive	−0.18048 nm/ RH%	0.72954 nm/°C	No	0.12 s	0.23 s	2024	[17]
Single-mode fiber and hollow capillary	Agar powder	0.95 nm/%RH	0.4333 nm/°C	Yes	0.88 s	1.17 s	2024	This work

4. Conclusion

In this paper, a flexible wearable sensor based on the FP structure is developed to successfully realize the monitoring of human breathing. The sensor utilizes the change of FP cavity length generated by the hygroscopicity of the agar film and eliminates the temperature crosstalk by cascading FBG to realize the accurate monitoring of human breathing. The experimental results show that the sensitivity of the sensor is 0.95 nm/%RH in the RH range of 60%RH-85%RH. The temperature sensitivity of the sensor varies nonlinearly from 30°C to 90°C, averaging 0.34 nm/°C over the range of 30°C to 55°C and 0.06 nm/°C over the range of 60°C to 90°C. In addition, the sensor has a fast response time (0.88 s) and recovery time (1.17 s) to human breathing as well as good resistance to vibration interference. The normal and deep breathing of nine subjects are monitored using the sensor, which demonstrates good sensing ability, repeatability and stability of the breathing pattern. Since the materials used to construct the sensor are safe and non-toxic, the proposed FPI sensor has the great advantage of low cost resistance to vibration and environmental compatibility, and will become a promising alternative for personal healthcare or clinical applications in the near future.

Funding. National Natural Science Foundation of China (62020106014, U2341211); Program of Marine Economy Development Special Fund (Six Marine Industries) under Department of Natural Resources of Guangdong Province (GDNRC [2024]16).

Disclosures. The authors declare no conflicts of interest.

Data availability. Data underlying the results presented in this paper are not publicly available at this time but may be obtained from the authors upon reasonable request.

References

1. X. Li, Y. Li, H. Wei, *et al.*, "A Review of Wearable Optical Fiber Sensors for Rehabilitation Monitoring," Sensors **24**(11), 3602 (2024).
2. S. Xiang, H. You, X. Miao, *et al.*, "An Ultra-Sensitive Multi-Functional Optical Micro/Nanofiber Based on Stretchable Encapsulation," Sensors **21**(22), 7437 (2021).
3. D. Jia, J. Chao, S. Li, *et al.*, "A Fiber Bragg Grating Sensor for Radial Artery Pulse Waveform Measurement," IEEE Trans. Biomed. Eng. **65**(4), 839–846 (2018).
4. R. Lu, X. Yue, Q. Yang, *et al.*, "Multi-node wearable optical sensor based on microfiber Bragg gratings," Opt. Express **32**(6), 8496–8505 (2024).
5. Y. Guo, X. Tong, Y. Shen, *et al.*, "Wearable Optical Fiber Beat Frequency Digital Sensing System for Real-Time Non-Invasive Multiple Human Physiological Parameters Monitoring," J. Lightwave Technol. **41**(9), 2911–2920 (2023).
6. R. Jha, P. Mishra, and S. Kumar, "Advancements in optical fiber-based wearable sensors for smart health monitoring," Biosens. Bioelectron. **254**, 116232 (2024).
7. J. Mathew, Y. Semenova, and G. Farrell, "A miniature optical breathing sensor," Biomed. Opt. Express **3**(12), 3325–3331 (2012).
8. W. Chen and X. Yan, "Progress in achieving high-performance piezoresistive and capacitive flexible pressure sensors: A review," J. Mater. Sci. Technol. **43**, 175–188 (2020).
9. C. Zhou, Q. Zhou, B. Wang, *et al.*, "High-sensitivity relative humidity fiber-optic sensor based on an internal-external Fabry-Perot cavity Vernier effect," Opt. Express **29**(8), 11854–11868 (2021).
10. M. Ghorat, G. B. Gharehpetian, H. Latifi, *et al.*, "High-Resolution FBG-Based Fiber-Optic Sensor with Temperature Compensation for PD Monitoring," Sensors **19**(23), 5285 (2019).
11. N. Zhao, Z. Wang, Z. Zhang, *et al.*, "High Sensitivity Optical Fiber Mach–Zehnder Refractive Index Sensor Based on Waist-Enlarged Bitaper," Micromachines **13**(5), 689 (2022).
12. S. Chen, C. Zhang, J. Wang, *et al.*, "A Fiber Bragg Grating Sensor Based on Cladding Mode Resonance for Label-Free Biosensing," Biosensors **13**(1), 97 (2023).
13. B. B. Du, D. X. Yang, X. Y. She, *et al.*, "MoS_2-based all-fiber humidity sensor for monitoring human breath with fast response and recovery," Sens. Actuators B-Chem. **251**, 180–184 (2017).
14. J. Yang, C. Guan, Z. Yu, *et al.*, "High sensitivity humidity sensor based on gelatin coated side-polished in-fiber directional coupler," Sens. Actuators B-Chem. **305**, 127555 (2020).
15. M. Bi, Y. Miao, W. Li, *et al.*, "Niobium carbide MXene-optics fiber-sensor for high sensitivity humidity detection," Appl. Phys. Lett. **120**(2), 021103 (2022).
16. Y. Li, X. Li, Y. Liu, *et al.*, "High sensitivity Mach-Zehnder interferometric fiber-optic humidity sensor based on multimode interference enhancement," Opt. Fiber Technol. **87**, 103891 (2024).
17. Y. X. Zhang, P. L. Liu, J. J. Yu, *et al.*, "Highly humidity sensitive Fabry-Perot interferometer sensor based on a liquid-solid microcavity for breath monitoring," Opt. Fiber Technol. **84**, 103761 (2024).
18. B. Wang, J. Tian, L. Hu, *et al.*, "High Sensitivity Humidity Fiber-Optic Sensor Based on All-Agar Fabry–Perot Interferometer," IEEE Sens. J. **18**(12), 4879–4885 (2018).
19. A. M. Shrivastav, D. S. Gunawardena, Z. Liu, *et al.*, "Microstructured optical fiber based Fabry–Pérot interferometer as a humidity sensor utilizing chitosan polymeric matrix for breath monitoring," Sci. Rep. **10**(1), 6002 (2020).
20. S. L. Khashin, S. A. Mohammed, and H. J. Taher, "Highly sensitive fiber optic humidity sensor based on polyvinyl alcohol Fabry-Perot," Opt. Continuum **1**(11), 2308–2318 (2022).
21. A. A. Noman, J. N. Dash, X. Cheng, *et al.*, "Hydrogel based Fabry-Pérot cavity for a pH sensor," Opt. Express **28**(26), 39640–39648 (2020).
22. Z. J. Khattak, M. Sajid, M. Javed, *et al.*, "Mass-Producible 2D Nanocomposite-Based Temperature-Independent All-Printed Relative Humidity Sensor," ACS Omega **7**(19), 16605–16615 (2022).
23. X. Ma, F. Zhao, B. Xu, *et al.*, "High-Sensitivity and Fast-Response Humidity Sensor Based on a Simple Fiber-Tip Interferometer With Thin Agarose Gel Coating," J. Lightwave Technol. **41**(21), 6824–6830 (2023).
24. E. Fujiwara, H. Oku, and C. M. B. Cordeiro, "Recent developments in agar-based optical devices," MRS Commun. **14**(3), 237–247 (2024).
25. Y. Zhao, R.-j. Tong, M.-Q. Chen, *et al.*, "Relative humidity sensor based on hollow core fiber filled with GQDs-PVA," Sens. Actuators B-Chem. **284**, 96–102 (2019).
26. J. Shi, D. Xu, W. Xu, *et al.*, "Humidity Sensor Based on Fabry–Perot Interferometer and Intracavity Sensing of Fiber Laser," J. Lightwave Technol. **35**(21), 4789–4795 (2017).

27. H. Chen, C. Jiang, X. Zhu, *et al.*, “A Parallel Optical Fiber Fabry–Perot Interferometer for Simultaneous Measurement of Relative Humidity and Temperature,” IEEE Sens. J. **22**(18), 17845–17853 (2022).
28. Y. Wang, C. Jiang, X. Guo, *et al.*, “High sensitivity relative humidity sensor based on two parallel-connected Fabry–Perot interferometers and Vernier effect,” Opt. Fiber Technol. **68**, 102767 (2022).
29. Y. Ma, S. Wang, X. Li, *et al.*, “Torsion and Temperature Sensor Based on Polished MSM Structure,” IEEE Photonics Technol. Lett. **32**(17), 1117–1120 (2020).
30. Y. Wu, G. Wang, X. Yu, *et al.*, “In-situ monitoring of charge and discharge process in supercapacitor with a micro-cavity Mach-Zehnder interferometer and a fiber Bragg grating,” Measurement **229**, 114428 (2024).
31. Y. Bai, Y. Miao, H. Zhang, *et al.*, “Simultaneous Measurement of Temperature and Relative Humidity Based on a Microfiber Sagnac Loop and MoS_2,” J. Lightwave Technol. **38**(4), 840–845 (2020).
32. Y. Bai, Y. Miao, H. Zhang, *et al.*, “Simultaneous measurement of relative humidity and temperature using a microfiber coupler coated with molybdenum disulfide nanosheets,” Opt. Mater. Express **9**(7), 2846–2858 (2019).
33. W. Wang, L. Jin, G. Shi, *et al.*, “Flexible wearable optical microfiber sensor for identifying bending direction and body temperature,” Opt. Laser Technol. **179**, 111281 (2024).